

## Supporting Information

### Turning Au Nanoclusters Catalytically Active for Visible-Light-Driven CO<sub>2</sub> Reduction through Bridging Ligands

Xiaofeng Cui,<sup>†, ‡, ¶</sup> Jin Wang,<sup>†, ‡</sup> Bing Liu,<sup>†, ⊥</sup> Shan Ling,<sup>¶</sup> Ran Long,<sup>‡</sup> and Yujie Xiong<sup>\*‡</sup>

<sup>‡</sup> *Hefei National Laboratory for Physical Sciences at the Microscale, iChEM  
(Collaborative Innovation Center of Chemistry for Energy Materials), School of  
Chemistry and Materials Science, and National Synchrotron Radiation Laboratory,  
University of Science and Technology of China, Hefei, Anhui 230026, P. R. China*

<sup>¶</sup> *Anhui Key Laboratory of Photoelectric-Magnetic Functional Materials, School of  
Chemistry and Chemical Engineering, Anqing Normal University, Anqing, Anhui  
246011, P. R. China*

<sup>⊥</sup> *School of Chemical and Material Engineering, Jiangnan University, Wuxi, Jiangsu  
214122, R. P. China*

*\*Corresponding author. E-mail: [yjxiong@ustc.edu.cn](mailto:yjxiong@ustc.edu.cn)*

<sup>†</sup>These authors contributed equally.

## 1. Experimental Procedure:

**Materials.** All used chemicals were analytical reagents without further purification. L-glutathione reduced (GSH,  $\geq 98\%$ ), 2-(N-morpholino) ethane sulfonic acid (MES,  $\geq 99\%$ ) 1-(3-dimethylaminopropyl)-3-ethylcarbodiimide hydrochloride (EDC,  $\geq 98\%$ ), N-hydroxysuccinimide (NHS,  $\geq 98\%$ ), L-cysteine (L-cys,  $\geq 98\%$ ), 3-mercaptopropionic acid (MPA,  $\geq 98\%$ ), and 2-methylimidazole ( $\geq 98\%$ ) were purchased from Aladdin Reagent Inc. Gold(III) chloride tetrahydrate ( $\text{HAuCl}_4 \cdot 4\text{H}_2\text{O}$ ,  $\geq 99.9\%$ ), iron(II) chloride tetrahydrate ( $\text{FeCl}_2 \cdot 4\text{H}_2\text{O}$ ,  $\geq 99\%$ ), cobalt(II) nitrate hexahydrate ( $\text{Co}(\text{NO}_3)_2 \cdot 6\text{H}_2\text{O}$ ,  $\geq 98.5\%$ ), nickel(II) nitrate hexahydrate ( $\text{Ni}(\text{NO}_3)_2 \cdot 6\text{H}_2\text{O}$ ,  $\geq 98\%$ ), copper(II) nitrate trihydrate ( $\text{Cu}(\text{NO}_3)_2 \cdot 3\text{H}_2\text{O}$ ,  $\geq 99\%$ ), zinc nitrate hexahydrate ( $\text{Zn}(\text{NO}_3)_2 \cdot 6\text{H}_2\text{O}$ ,  $\geq 99\%$ ), and triethanolamine (TEOA,  $\geq 99\%$ ) were obtained from Sinopharm Chemical Reagent Co., Ltd.).

**Synthesis of Au-GSH NCs.** Au-GSH nanoclusters (NCs) were synthesized by modifying a protocol reported by Louet al.<sup>S1</sup> First, 48.5 mg of  $\text{HAuCl}_4 \cdot 4\text{H}_2\text{O}$  was dissolved in 30 mL of deionized water at room temperature in a 50-mL round-bottom flask. Subsequently, 50 mg of L-glutathione was introduced to the flask with stirring, which was stirred until the solution turned colorless (about 1.5 h). The flask was then heated to 70 °C in an oil bath with constant stirring. After 24 h, this flask was removed from the oil bath and allowed to cool to room temperature. The nanoclusters were purified by adding 30 mL of acetonitrile to 10 mL of the as-prepared Au-GSH NCs solution. This solution was mixed well and centrifuged at 8,000 rpm for 5 min. Finally, the supernatant was discarded, and the remaining crystals were washed three times with the mixture of deionized water and acetonitrile (1:3 volume ratio). The purified Au-GSH NCs were redispersed in 10 mL of deionized water for further use.

**Encapsulation of  $\text{Au}_c\text{-C-Co}$  with ZIF-8 framework ( $\text{Au}_c\text{-C-Co@ZIF-8}$ ).** The encapsulation process was performed in aqueous solution.<sup>S2</sup> 3.5 g of 2-methylimidazole was dissolved in 90 mL of deionized water and cooled to 0 °C in

ice-water bath. 0.2 g of  $\text{Zn}(\text{NO}_3)_2 \cdot 6\text{H}_2\text{O}$  was added into 10 mL of pristine  $\text{Au}_c\text{-C-Co}$  solution ( $1 \text{ g} \cdot \text{mL}^{-1}$ ), which was also cooled to  $0^\circ\text{C}$  after ultrasonic dispersion for 30 min. Subsequently, the 10-mL mixture was rapidly injected into aqueous 2-methylimidazole solution under vigorous stirring. After a 5-min reaction, the resulting pale yellow precipitate was centrifuged at 8,000 rpm for 5 min, washed with ice water, and vacuum dried at  $60^\circ\text{C}$ .

**Functionalization of Au-GSH NCs with 3-mercaptopropionic acid (MPA).** This protocol is similar to the modification of Au-GSH NCs with L-cysteine. 35  $\mu\text{L}$  of MPA was added into 10 mL of MES buffer ( $3.9 \text{ mg} \cdot \text{mL}^{-1}$ ) in a 50-mL round-bottom flask, which was then heated to  $65^\circ\text{C}$ . Subsequently, 6 mg of EDC and 1.6 mg of NHS were added as catalysts to form amide bond between the carboxylic groups of MPA and the amino groups of Au-GSH NCs. After stirring for 15 min, 10 mL of Au-GSH NCs dispersion ( $1 \text{ g} \cdot \text{L}^{-1}$ ) was added in. The final mixture was stirred at  $65^\circ\text{C}$  for 6 h. The resulting MPA-modified Au-GSH NCs ( $\text{Au}_c\text{-MPA}$ ) were collected by centrifugation at 8,000 rpm for 5 min and washed with deionized water three times. Finally, 5 mL of deionized water was added into the purified  $\text{Au}_c\text{-MPA}$ , and 10  $\mu\text{L}$  of NaOH (30% wt) was added timely for better dispersing  $\text{Au}_c\text{-MPA}$  in aqueous solution.

**Synthesis of  $\text{Au}_{25}(\text{SG})_{18}$  NCs.**  $\text{Au}_{25}(\text{SG})_{18}$  NCs were synthesized by following the protocol in literature.<sup>S2, S3</sup> GSH (0.1535 g, 0.5 mmol) was dissolved in methanol solution of  $\text{HAuCl}_4$  (25 mL, 0.25 mmol), and the resulting mixture was cooled to  $0^\circ\text{C}$  for 30 min. Fresh  $\text{NaBH}_4$  aqueous solution (6.25 mL, 0.2 M, cooled to  $0^\circ\text{C}$ ) was injected rapidly into the mixture above under vigorous stirring. After reaction in ice bath for 3 h, the resulting precipitate was collected by centrifugation and washed with methanol three times. The chemical etching was performed by re-dissolving the obtained dark-brown precipitate in GSH aqueous solution (7 mL, 130 mg) and stirring at 328 K for 12 h. Subsequently, the solution was centrifuged at 9,500 rpm for 5 min to remove large particles, and the supernatants were loaded into a dialysis bag with a

molecular-weight cut-off of 3 kDa for 2 days to remove small molecular impurities.

**Functionalization of Au<sub>25</sub>(SG)<sub>18</sub> with L-cysteine.** This protocol is similar to the modification of Au-GSH NCs with L-cysteine except the reaction time was shortened to 30 min.

## **2. Sample Characterizations:**

Matrix-assisted laser desorption/ionization time-of-flight (MALDI-TOF) mass spectrometry was carried out on an AB SCIEX 5800 MALDI TOF system operated in the negative ion mode.

Prior to electron microscopy characterizations, a drop of the ethanol suspension of particles was placed on a piece of carbon-coated copper grid and dried under ambient conditions. Transmission electron microscopy (TEM) and high-resolution TEM (HRTEM) images were taken on a JEOL JEM-2100F field-emission high-resolution transmission electron microscope operated at 200 kV.

Fourier-transform infrared spectroscopy (FTIR) spectrum measurements were performed using a Bruker IFS 66v Fourier-transform spectrometer equipped with a Harrick diffuse reflectance accessory at the Infrared Spectroscopy and Microspectroscopy Endstation (BL01B).

X-ray photoelectron spectra (XPS) were collected on an ESCA Lab 250 X-ray photoelectron spectrometer, using nonmonochromatized Al-K $\alpha$  X-ray as the excitation source.

UV-vis diffused reflectance spectra were recorded on a UV-Vis spectrophotometer (Hitachi U-4100) with the integration sphere diffuse reflectance attachment.

UV-vis absorption spectra were recorded on a Shimadzu 2501 PC UV-vis

spectrophotometer.

$^1\text{H}$  nuclear magnetic resonance (NMR) spectra were measured at 293 K with a frequency of 15 MHz using a Bruker AVANCE AV400 NMR spectrometer.

The content of ligands in solution was determined on an Agilent 1260 Infinity II High-Performance Liquid Chromatography (HPLC). The reacted solution was mixed with 4 times methanol precipitator, and then centrifuged to remove Au NCs. The mobile phase was methanol:H<sub>2</sub>O = 4:1 with a flow rate of 1.0 mL·min<sup>-1</sup>.

The concentrations of metal elements were measured as follows: the samples were dissolved with a mixture of HCl and HNO<sub>3</sub> (3:1, volume ratio) which was then diluted with deionized water. The concentrations of metals were then measured with a PerkinElmer Optima 8300 inductively-coupled plasma optical emission spectrometry (ICP-OES)

Room-temperature electron spin resonance (ESR) spectra were collected using a JEOL JES-FA200 ESR spectrometer (300 K, 9.063 GHz, X-band). A 300-W Xe lamp was used as an *in-situ* light source.

The steady-state photoluminescence (PL) spectra were collected on a photoluminescence spectrometer (Hitachi F-4500) with a 150-W Xe lamp as the excitation source, and the excitation wavelength was set at 450 nm. The PL decay spectra were recorded on a photoluminescence spectrometer (FLS980, Edinburgh Instruments Ltd.) through a 455-nm excitation wavelength with the time-correlated single-photon counting (TCSPC) mode. The decay curves were fitted using a triexponential decay kinetic equation:<sup>S4</sup>

$$A(t) = A_1 e^{(-\frac{t}{\tau_1})} + A_2 e^{(-\frac{t}{\tau_2})} + A_3 e^{(-\frac{t}{\tau_3})} \quad (\text{S1})$$

The average PL lifetimes ( $\tau$ ) were calculated according to the following equation:<sup>S4</sup>

$$\tau = (A_1\tau_1^2 + A_2\tau_2^2 + A_3\tau_3^2) / (A_1\tau_1 + A_2\tau_2 + A_3\tau_3) \quad (S2)$$

The contributions of the components with fast decay times ( $\tau_i\%$ ) was calculated through the following equation:<sup>S5</sup>

$$\tau_i \% = A_i / (A_1 + A_2 + A_3) \quad (S3)$$

### 3. DFT calculation:

All the spin-polarized density functional theory (DFT) calculations were performed using the Vienna *ab initio* simulation package (VASP).<sup>S6, S7</sup> The projector-augmented wave method was used to represent core-valence interactions.<sup>S8</sup> Valence electrons were described by a plane wave basis with an energy cutoff of 400 eV. The generalized gradient approximation with the Perdew-Burke-Ernzerhof functional was used to model electronic exchange and correlation.<sup>S9</sup> Electron smearing was employed via the Methfessel-Paxton technique with a smearing width consistent to 0.2 eV. Optimized structures were obtained by minimizing the forces on each cation until they were less than 0.05 eV·Å<sup>-1</sup>. Transition states (TSs) for the elementary reactions were located using the climbing-image nudged elastic band method,<sup>S10, S11</sup> and were confirmed as having a single imaginary frequency. Energy barriers ( $E_{\text{bar}}$ ) were calculated as the energy difference between the transition and initial states.

The adsorption energy was defined as:<sup>S12</sup>

$$E_{\text{ads}} = E(\text{adsorbate+surface}) - E(\text{adsorbate}) - E(\text{surface}) \quad (S4)$$

where  $E(\text{adsorbate+surface})$  is the total energy of the adsorbate interacting with the surface,  $E(\text{adsorbate})$  and  $E(\text{surface})$  are the energies of the free adsorbate in gas phase and on bare surface, respectively. A negative value for  $E_{\text{ads}}$  corresponds to exothermic adsorption, and more negative values suggest stronger binding.

The *d*-band center ( $\epsilon_d$ ) of surface atoms was calculated using the following equation:<sup>S13</sup>

$$\varepsilon_d = \frac{\int_{-\infty}^{E_f} E \rho_d(E) dE}{\int_{-\infty}^{E_f} \rho_d(E) dE} \quad (\text{S5})$$

where  $E_f$  is the Fermi energy,  $E$  is the energy with respect to the Fermi level ( $E_f$ ), and  $\rho_d(E)$  is the density of states projected onto five  $d$  orbits of the surface atoms at energy  $E$ .

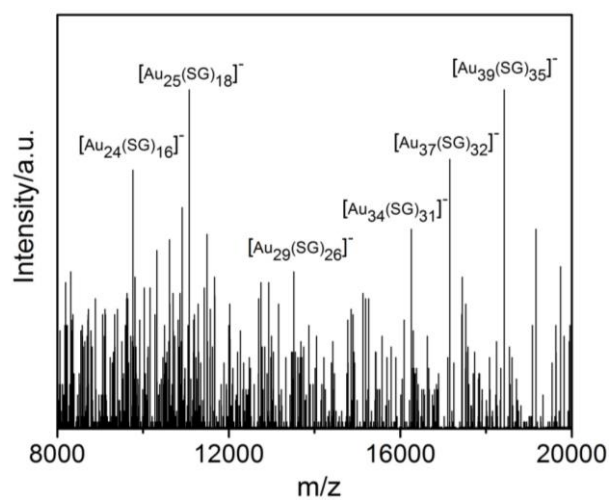


**Figure S1.** MALDI-TOF mass spectrum of Au-GSH NCs.

MALDI-TOF mass spectrum (Figure S1) shows that the Au NCs have a size distribution ranging from Au<sub>24</sub> to Au<sub>39</sub>.



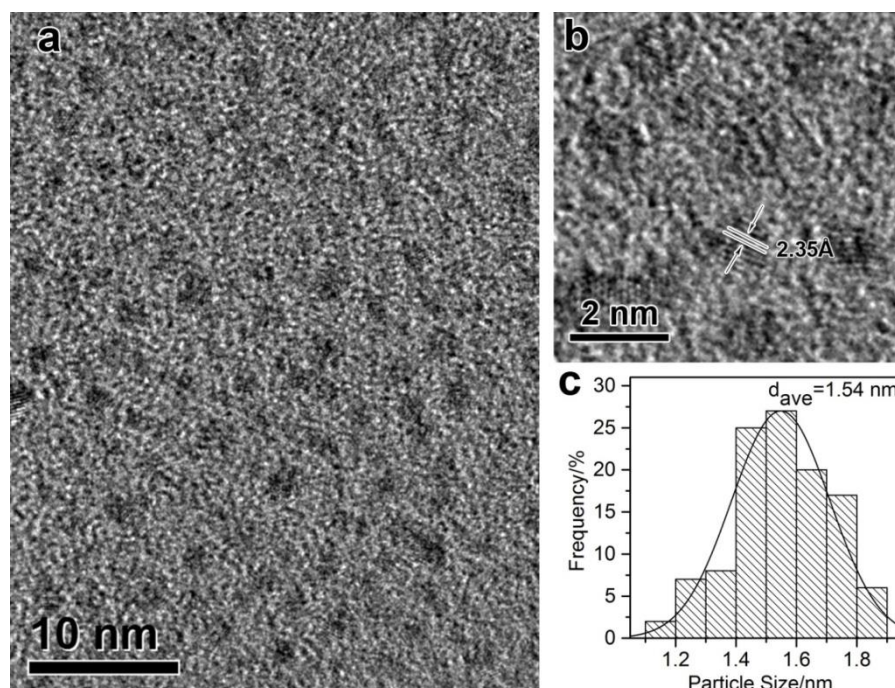


**Figure S2.** (a) TEM, (b) HRTEM images and (c) particle size distribution histogram of L-cys-modified Au-GSH NCs (Au<sub>c</sub>-C).

As revealed by TEM (Figure S2a), Au NCs have an average size of 1.53 nm after the surface modification process, which appear similarly to the pristine Au NCs. HRTEM image (Figure S2b) shows that the gold cores in the NCs are of a face-centered cubic (*fcc*) structure with a lattice spacing of 2.35 Å, consistent with the previously reported feature for Au-GSH NCs.<sup>S1</sup> This indicates that the structure of NCs has been well retained after the functionalization.

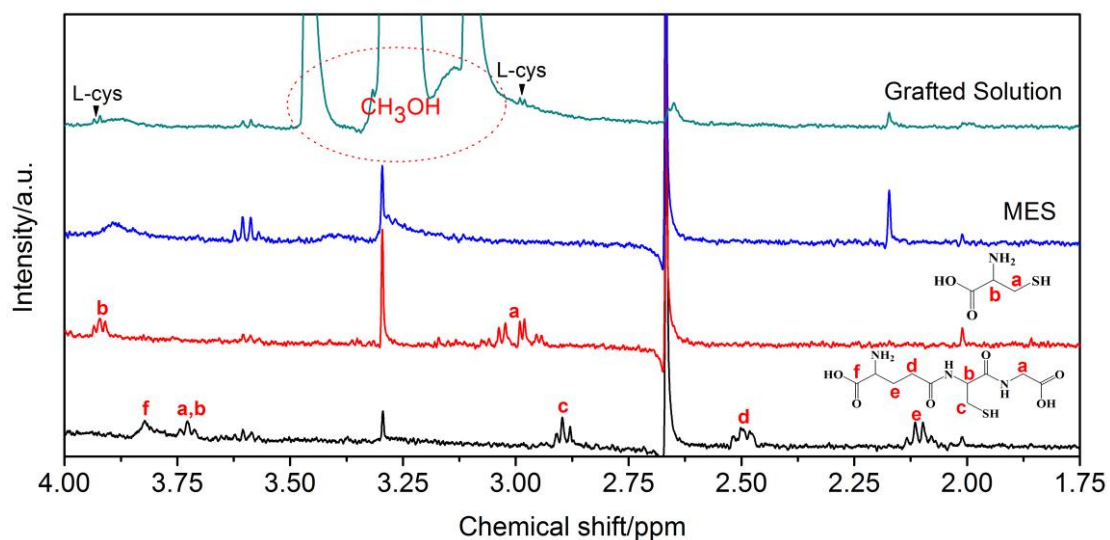


**Figure S3.**  $^1\text{H}$  NMR spectra of the reaction solution after modifying Au-GSH NCs with L-cys for 6 h, in reference to GSH, L-cys and MES.

The  $^1\text{H}$  NMR spectra in Figure S3 show that no free GSH can be detected in the solution after the reaction of modifying Au-GSH NCs with L-cys for 6 h. As such, the ligand exchange between the L-cys and Au-GSH NCs should be negligible in this system.

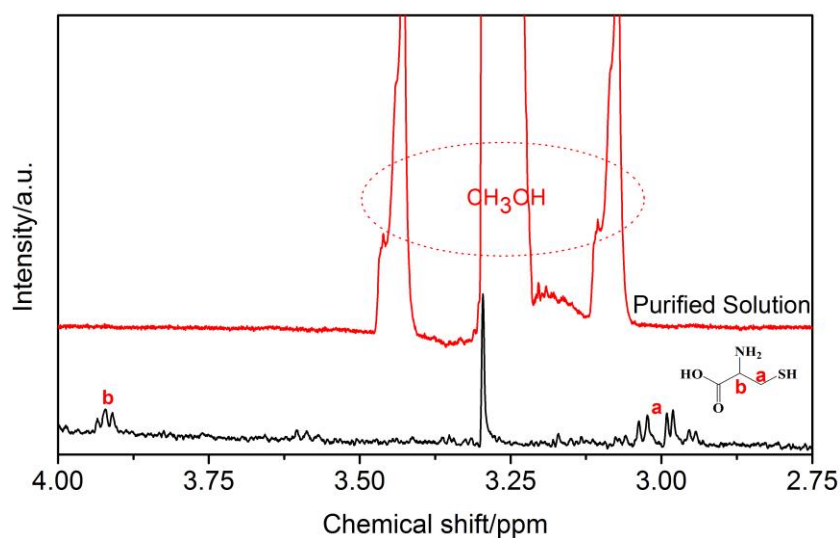


**Figure S4.**  $^1\text{H}$  NMR spectra of the fully purified solution of  $\text{Au}_c\text{-C}$ , in reference to L-cys.

The  $^1\text{H}$  NMR spectra in Figure S4 show that no free L-cys or GSH can be detected in the solution after fully purifying the functionalized  $\text{Au}_c\text{-C}$ . This indicates that the purification of  $\text{Au}_c\text{-C}$  has been successfully achieved.

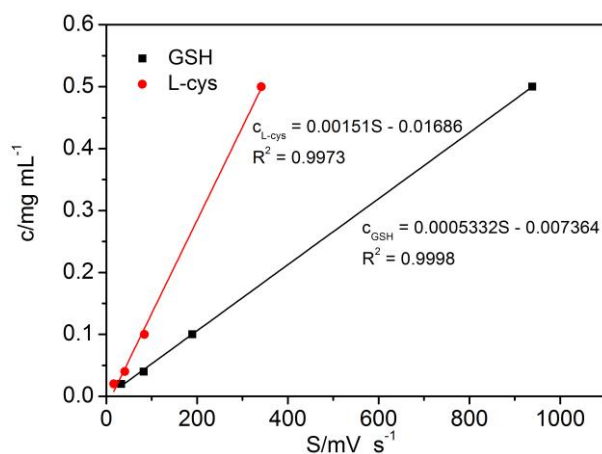


**Figure S5.** Standard curves for the quantitative analysis on the contents of GSH and L-cys obtained by HPLC.

Based on the standard curves (Figure S5), we can quantitatively analyze the amount of L-cys in the solution after the reaction of modifying Au-GSH NCs with L-cys through HPLC. It turns out that 40% of L-cys has grafted to the Au-GSH NCs. After the functionalization, the molar ratio of GSH to grafted L-cys is about 1:0.81.

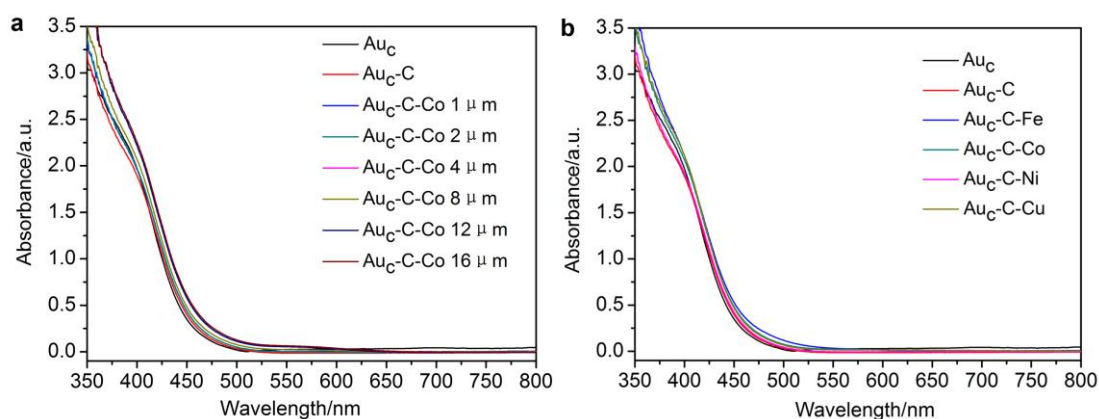


**Figure S6.** (a) UV-vis absorption spectra of  $Au_C$ ,  $Au_C-C$  and  $Au_C-C$  grafted with different amounts of  $Co^{2+}$  cations. (b) UV-vis absorption spectra of  $Au_C-C-Fe$ ,  $Au_C-C-Co$ ,  $Au_C-C-Ni$  and  $Au_C-C-Cu$  with the same amount of metal cations ( $4 \mu mol$ ), in reference to  $Au_C$  and  $Au_C-C$  at the same concentration of Au NCs.

The absorption spectrum (Figure S4a) indicates that Au-GSH NCs are excellent absorbers to harvest visible light up to 500 nm.

The light absorption is well maintained upon the modification of Au-GSH NCs with L-cys (Figure S6a,  $Au_C$  versus  $Au_C-C$ ). This suggests that the Au-GSH NCs have not aggregated after the ligand modification.

The absorption profile has not been altered by grafting various metal cations (Figure S4b), even when the concentration of metal cations is further increased (Figure S4a).

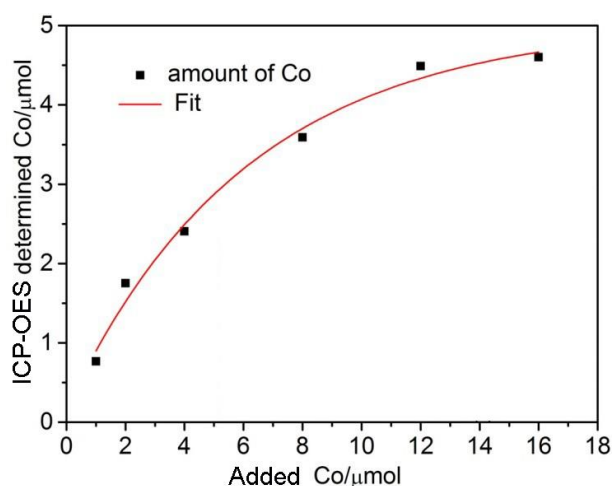


**Figure S7.** The amounts of  $\text{Co}^{2+}$  cations that have been anchored to 10 mg of  $\text{Au}_n\text{-C}$  at different amounts of added  $\text{Co}^{2+}$ , determined by ICP-OES.

The amounts of anchored Co have been determined by ICP-OES through the following procedure: a certain amount of  $\text{Co}^{2+}$  (0.1 M) was added to 10 mL of  $\text{Au}_n\text{-C}$  dispersion ( $1 \text{ g}\cdot\text{L}^{-1}$ ) under vigorous stirring. After stirring for 30 min, 30 mL of acetonitrile was added to the dispersion, centrifuged and washed with the mixture of deionized water and acetonitrile (1:3 volume ratio) once.

Figure S7 shows the plot for the amount of  $\text{Co}^{2+}$  anchored to  $\text{Au}_n\text{-C}$  *versus* the amount of added  $\text{Co}^{2+}$ . The plot displays a nearly linear relationship at relatively low concentrations of  $\text{Co}^{2+}$ , as the abundant uncoordinated thiols in  $\text{Au}_n\text{-C}$  can be coordinated with  $\text{Co}^{2+}$ . When the added amount of  $\text{Co}^{2+}$  is increased beyond  $4 \mu\text{mol}$ , the rate of anchoring  $\text{Co}^{2+}$  to  $\text{Au}_n\text{-C}$  is gradually reduced. This suggests that the exposed thiols have been largely coordinated with  $\text{Co}^{2+}$ . Beyond this point, further addition of  $\text{Co}^{2+}$  to the system will result in a relatively high concentration of free  $\text{Co}^{2+}$  in the solution.

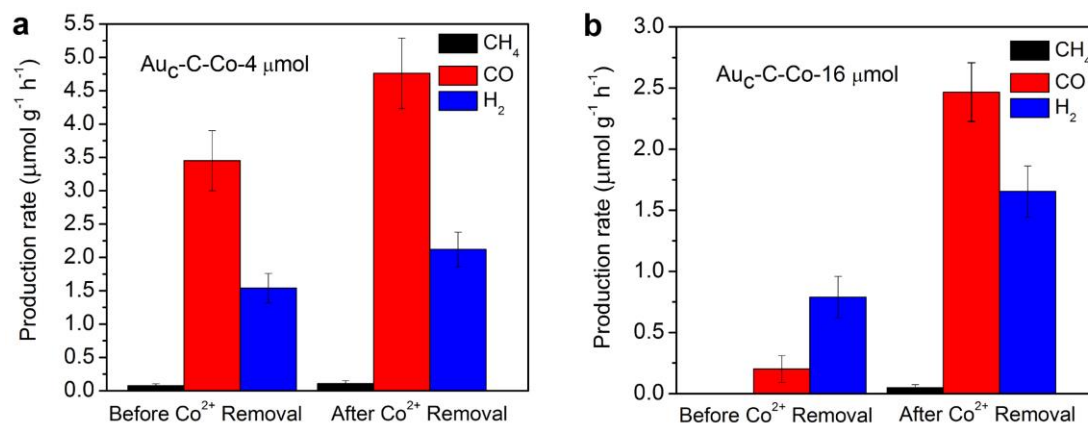


**Figure S8.** Average production rates of  $\text{CH}_4$ ,  $\text{CO}$  and  $\text{H}_2$  in light-driven  $\text{CO}_2$  reduction with  $\text{H}_2\text{O}$  in the presence of TEOA, catalyzed by (a)  $\text{Au}_\text{C}\text{-C-Co-4 } \mu\text{mol}$  and (b)  $\text{Au}_\text{C}\text{-C-Co-16 } \mu\text{mol}$  before and after removing free  $\text{Co}^{2+}$  from the reaction solution through dialysis.

Excess free metal cations are detrimental to photocatalytic reactions as they can work as a shuttle redox mediator for the recombination of photogenerated electrons with holes. To prove this assumption, we assess the activity of the samples ( $\text{Au}_\text{C}\text{-C-Co-4 } \mu\text{mol}$  and  $\text{Au}_\text{C}\text{-C-Co-16 } \mu\text{mol}$ ) after removing the free  $\text{Co}^{2+}$  through dialysis (Figure S8). After removing the free  $\text{Co}^{2+}$ , both the photocatalytic activities of  $\text{Au}_\text{C}\text{-C-Co-4 } \mu\text{mol}$  and  $\text{Au}_\text{C}\text{-C-Co-16 } \mu\text{mol}$  can be improved. It confirms that the free  $\text{Co}^{2+}$  lowers the photocatalytic activity, which may become more severe in the case of high-concentration  $\text{Co}^{2+}$  loading due to ion leaching.

It is worth pointing out that the activity for  $\text{CO}_2$  reduction is more affected by free  $\text{Co}^{2+}$  than  $\text{H}_2$  generation. This difference can be attributed to the reaction barriers of proton reduction and  $\text{CO}_2$  reduction. It is well known that proton reduction can more easily take place than  $\text{CO}_2$  reduction (the rate-limiting step for  $\text{CO}_2$  reduction  $\text{CO}_2 + \text{e}^- \rightarrow \text{CO}_2^{\cdot-}$ ,  $-1.85\text{V}$  versus SHE; water reduction  $2\text{H}_2\text{O}(l) + 2\text{e}^- \rightarrow \text{H}_2(g) + 2\text{OH}^-(aq)$ ,  $-0.414\text{ V}$  versus SHE).

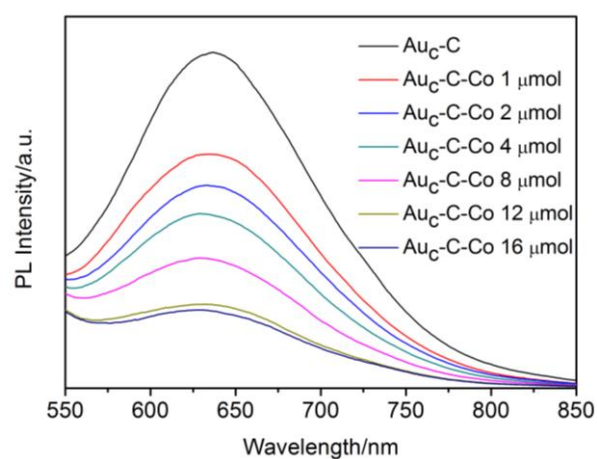


**Figure S9.** The luminescent photoemission ( $\lambda_{\text{ex}}=450$  nm) spectra of Au-GSH NCs modified with L-cys ( $\text{Au}_c\text{-C}$ ) and  $\text{Au}_c\text{-C}$  grafted with different amounts of  $\text{Co}^{2+}$  cations ( $\text{Au}_c\text{-C-Co}$ ) in aqueous solution ( $1 \text{ g}\cdot\text{L}^{-1}$ ).

Strong photoemission of L-cys modified Au-GSH NCs ( $\text{Au}_c\text{-C}$ ) are observed with maxima around 630 nm (Figure S9). The PL of  $\text{Au}_c\text{-C}$  is gradually quenched by increasing the loading amounts of  $\text{Co}^{2+}$  cations in  $\text{Au}_c\text{-C-Co}$ .



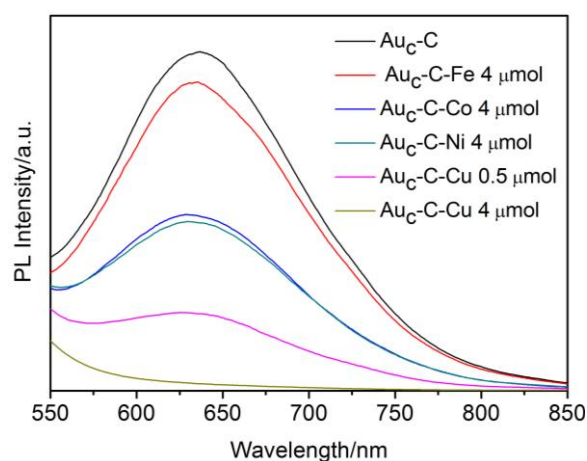


**Figure S10.** The luminescent photoemission ( $\lambda_{\text{ex}}=450$  nm) spectra of Au-GSH NCs modified with L-cys ( $\text{Au}_c\text{-C}$ ) and  $\text{Au}_c\text{-C}$  grafted with various metal cations ( $\text{Fe}^{2+}$ ,  $\text{Co}^{2+}$ ,  $\text{Ni}^{2+}$  and  $\text{Cu}^{2+}$ ) ( $\text{Au}_c\text{-C-M}$ ) in aqueous solution.

Various metal cations display different quenching effects on the PL of Au NCs (Figure S10). It is evident that the addition of  $\text{Cu}^{2+}$  cations shows the most remarkable quenching effect (100%), while  $\text{Co}^{2+}$  and  $\text{Ni}^{2+}$  quench the PL 52.1% and 49.7% at the same amount of metal cations (4  $\mu\text{mol}$ ), respectively. In contrast, no apparent quenching can be observed for the addition of  $\text{Fe}^{2+}$ .

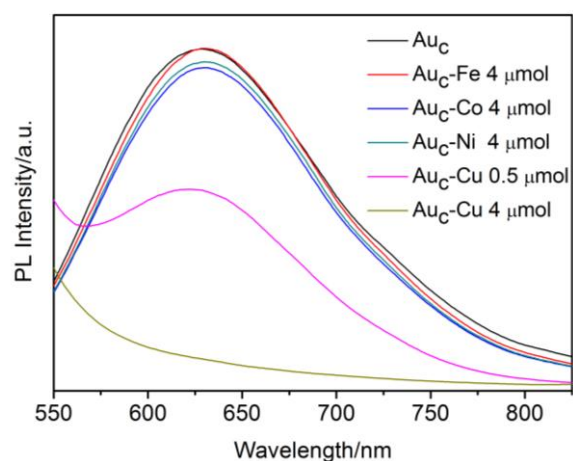


**Figure S11.** The luminescent photoemission ( $\lambda_{\text{ex}}=450$  nm) spectra of the unmodified Au-GSH NCs ( $\text{Au}_c$ ) mixed with various metal cations ( $\text{Fe}^{2+}$ ,  $\text{Co}^{2+}$ ,  $\text{Ni}^{2+}$  and  $\text{Cu}^{2+}$ ) ( $\text{Au}_c\text{-M}$ ) in aqueous solution ( $1 \text{ g}\cdot\text{L}^{-1}$ ).

In the absence of bridging ligands, the PL of the unmodified Au-GSH NCs ( $\text{Au}_c$ ) whose strong photoemission exhibits a maxima around 630 nm can hardly be quenched by the addition of  $\text{Fe}^{2+}$ ,  $\text{Co}^{2+}$  and  $\text{Ni}^{2+}$  cations (Figure S11). The only exception is the distinct quenching observed for the addition of  $\text{Cu}^{2+}$  cations.

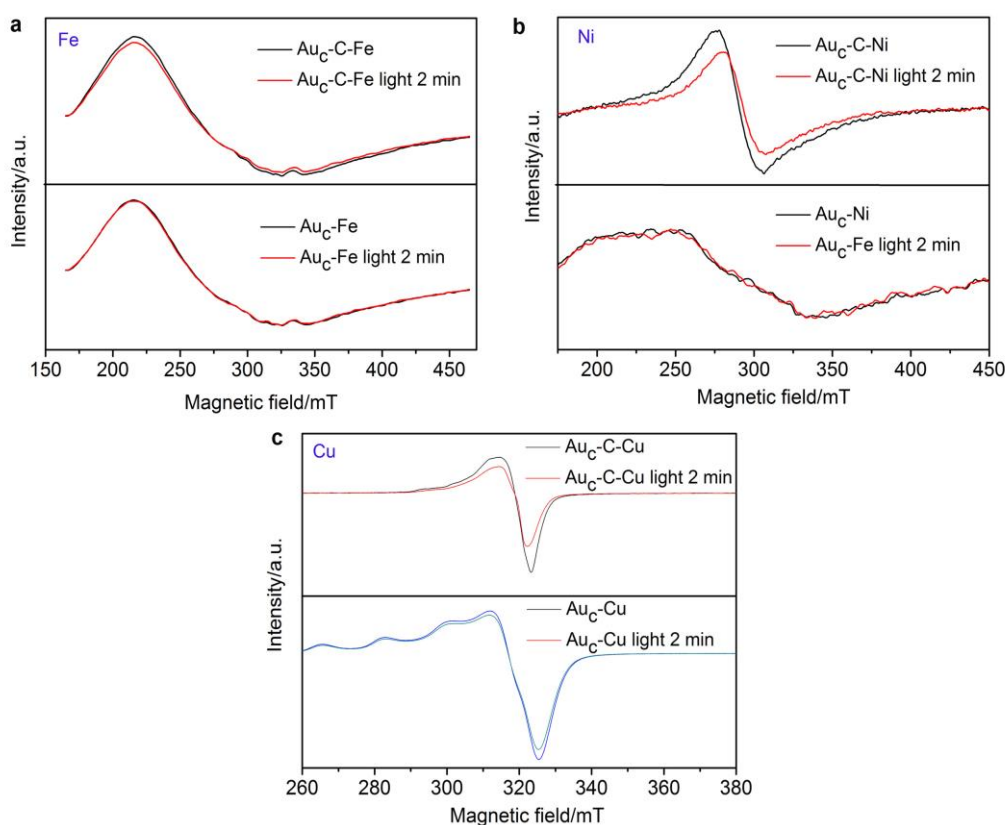


**Figure S12.** ESR spectra of (a) Au<sub>c</sub>-Fe (lower) and Au<sub>c</sub>-C-Fe (upper), (b) Au<sub>c</sub>-Ni (lower) and Au<sub>c</sub>-C-Ni (upper), and (c) Au<sub>c</sub>-Cu (lower) and Au<sub>c</sub>-C-Cu (upper) in dark or under light irradiation for 2 min.

The Au<sub>c</sub>-M samples for ESR measurements are prepared by following the procedures below. 0.1-g samples are dispersed in 0.5-mL aqueous solution, into which 30  $\mu$ L of NaOH (30 wt.%) is added timely for better dispersion. Finally, 40- $\mu$ L aqueous dispersion of metal cations (Fe<sup>2+</sup>, Co<sup>2+</sup>, Ni<sup>2+</sup> or Cu<sup>2+</sup>, 0.1 mol·L<sup>-1</sup>) is added under vigorous shaking. The final aqueous solution is dried by freeze drying.

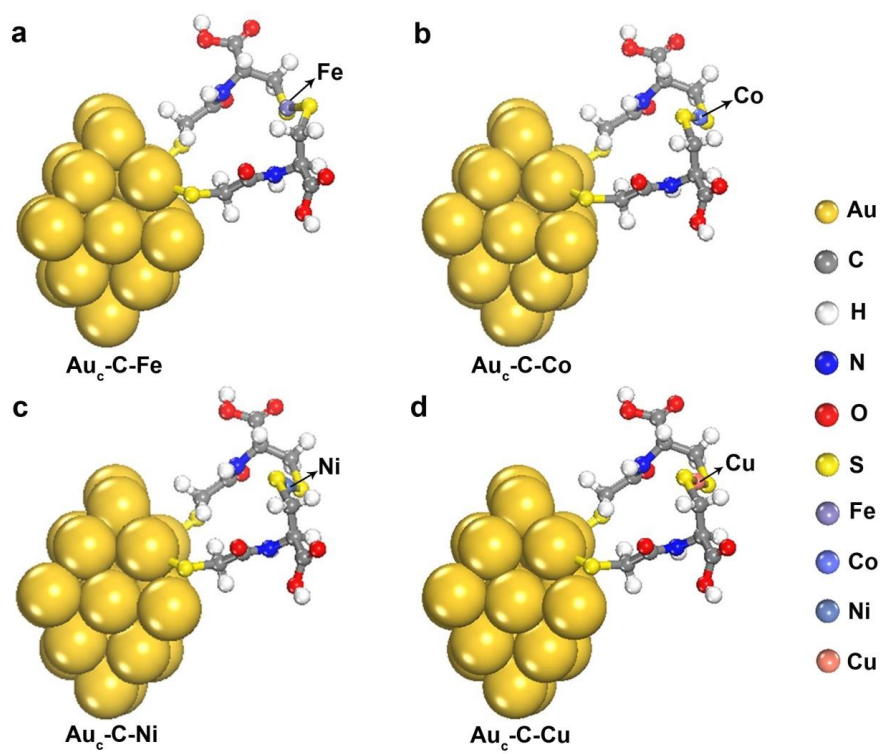


**Figure S13.** Calculated structures of Au-GSH NCs modified with L-cys and grafted with (a) Fe<sup>2+</sup>, (b) Co<sup>2+</sup>, (c) Ni<sup>2+</sup> and (d) Cu<sup>2+</sup> (Au<sub>c</sub>-C-M).

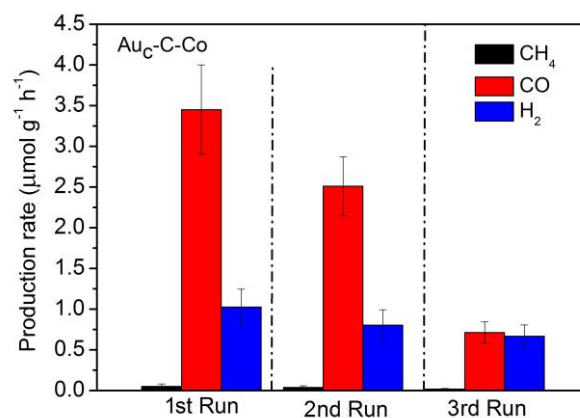


**Figure S14.** Average production rates of CH<sub>4</sub>, CO and H<sub>2</sub> in light-driven CO<sub>2</sub> reduction with H<sub>2</sub>O in the presence of TEOA, catalyzed by Au<sub>c</sub>-C-Co in 3 successive 3-hour cycles.

The NC-based catalysts exhibit frustrating photostability in the cycling test, and become nearly inactive after the 3 cycles (Figure S14).

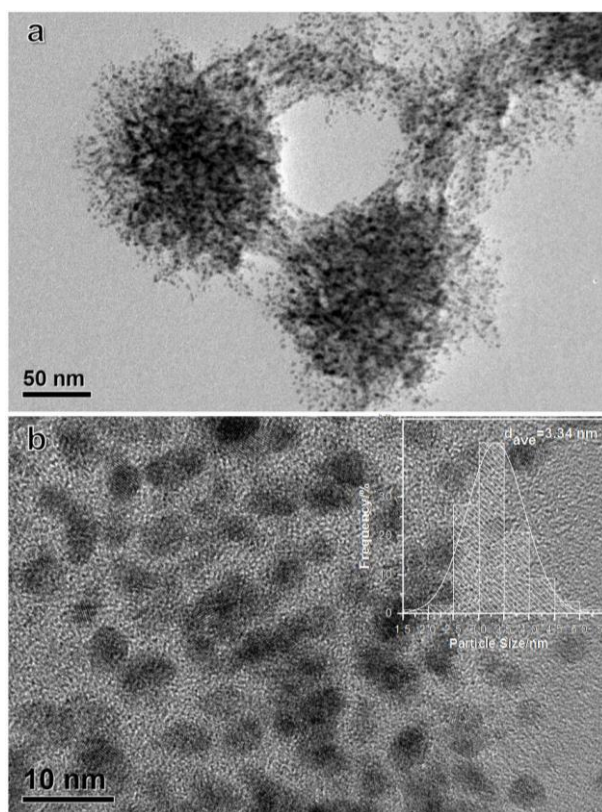


**Figure S15.** (a) TEM and (b) HRTEM images of Au<sub>c</sub>-C-Co after 9-hour photocatalytic CO<sub>2</sub> reduction. The inset of panel b shows the corresponding size distribution diagram.

TEM characterization (Figure S15) reveals that Au NCs have been aggregated and grown from 1.53 nm up to Au nanoparticles with an average diameter of 3.34 nm after the 3 cycles.

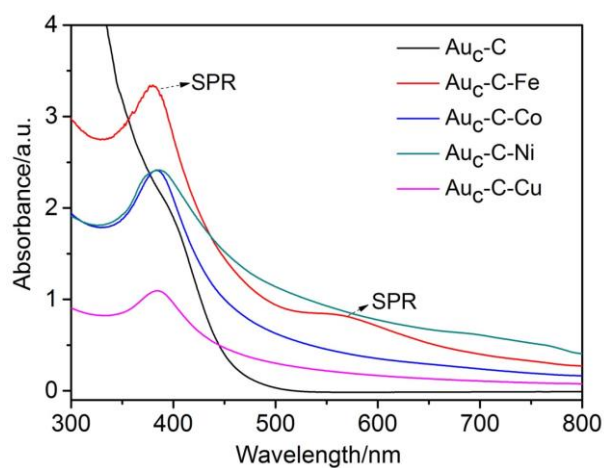


**Figure S16.** UV-vis absorption spectra of Au<sub>c</sub>-C, Au<sub>c</sub>-C-Fe, Au<sub>c</sub>-C-Co, Au<sub>c</sub>-C-Ni and Au<sub>c</sub>-C-Cu after 9-hour photocatalytic CO<sub>2</sub> reduction.

After the 9-hour photocatalytic CO<sub>2</sub> reduction, surface plasmon resonance (SPR) peaks for Au nanoparticles emerge in the UV-vis absorption spectra (Figure S16). This further illustrates that Au NCs have been extensively transformed into nanoparticles.

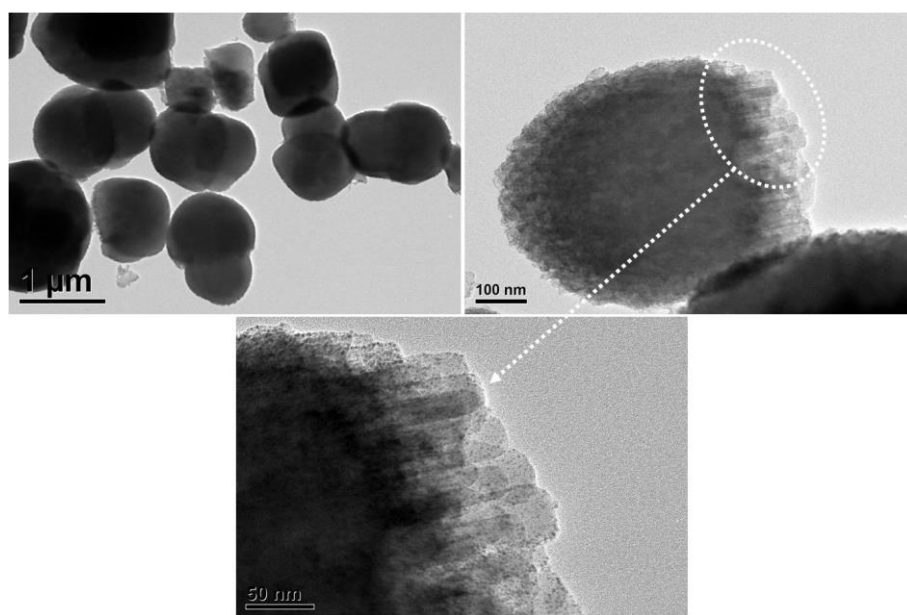


**Figure S17.** TEM images of Au<sub>c</sub>-C-Co encapsulated with ZIF-8 (Au<sub>c</sub>-C-Co@ZIF-8).

To prevent NC agglomeration and enhance photostability, we employ Zn(2-methylimidazole)<sub>2</sub> (ZIF-8) as an encapsulation shell to protect Au<sub>c</sub>-C-Co (Figure S17).



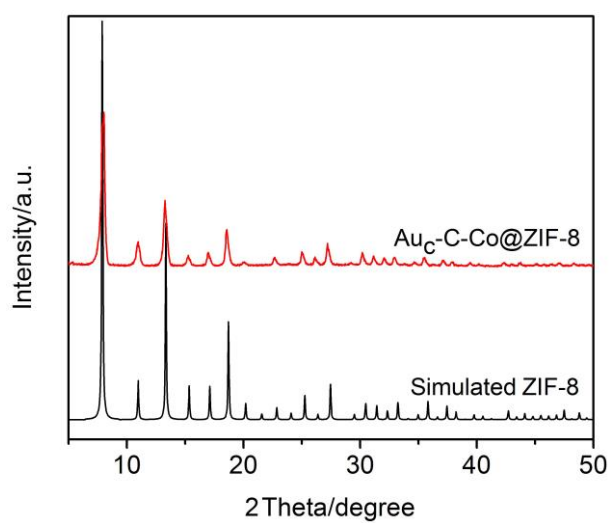


**Figure S18.** XRD pattern of Au<sub>c</sub>-C-Co@ZIF-8.

The powder XRD pattern (Figure S18) displays strong diffraction peaks at  $2\theta=7.4$ ,  $12.7$  and  $18.0^\circ$ , which agree well with the simulated pattern for ZIF-8 single crystal with the typical SOD structure.

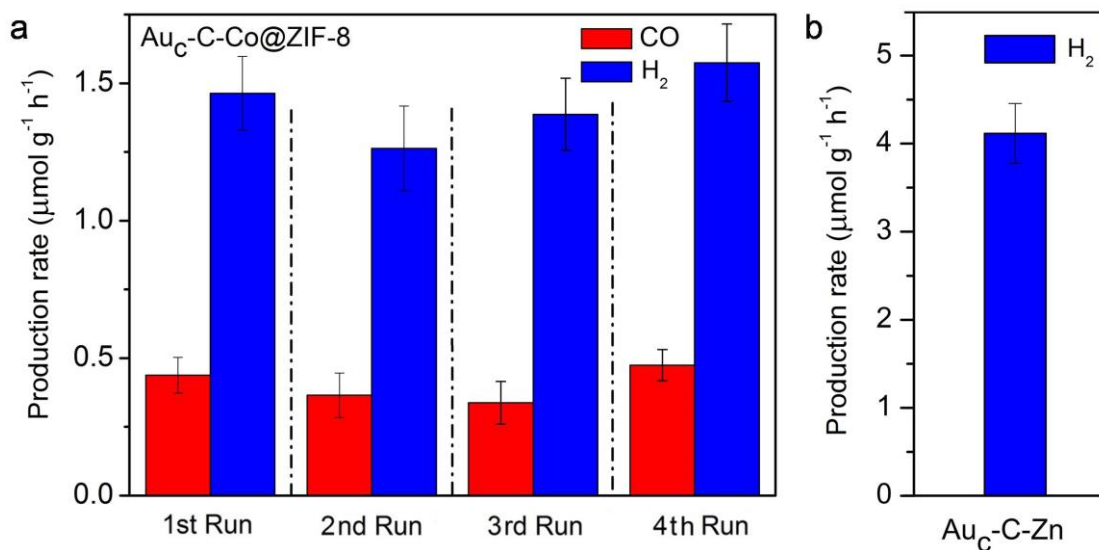


**Figure S19.** (a) Average production rates of CH<sub>4</sub>, CO and H<sub>2</sub> in light-driven CO<sub>2</sub> reduction with H<sub>2</sub>O in the presence of TEOA, catalyzed by Au<sub>C</sub>-C-Co@ZIF-8 in 4 successive 3-hour cycles. (b) Average production rates of H<sub>2</sub> in light-driven CO<sub>2</sub> reduction with H<sub>2</sub>O in the presence of TEOA, catalyzed by Au<sub>C</sub>-C-Zn.

As shown in Figure S19a, no obvious activity decay is observed for Au<sub>C</sub>-C-Co@ZIF-8 during four 3-hour reaction cycles. However, the activity and CO selectivity are lowered after the ZIF-8 encapsulation. Most likely, the selectivity is reduced by the presence of Zn in ZIF-8. To prove this hypothesis, we prepare a sample by grafting Zn<sup>2+</sup> to Au<sub>C</sub>-C (Au<sub>C</sub>-C-Zn). As shown in Figure S19b, the Au<sub>C</sub>-C-Zn sample shows the high selectivity of H<sub>2</sub> production in the photocatalytic system of CO<sub>2</sub> and H<sub>2</sub>O. This demonstrates that the Zn in ZIF-8 may produce H<sub>2</sub> to reduce the CO selectivity by Au<sub>C</sub>-C-Co@ZIF-8.

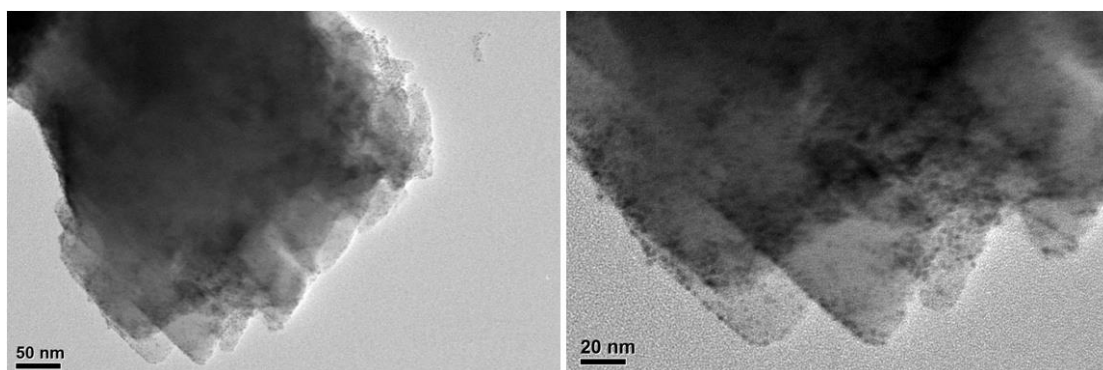


**Figure S20.** TEM images of Au<sub>x</sub>-M-Co@ZIF-8 after 12-hour photocatalytic CO<sub>2</sub> reduction.

After the 12-hour photocatalytic CO<sub>2</sub> reduction, the ZIF-8 coating is well maintained as indicated by TEM (Figure S20).

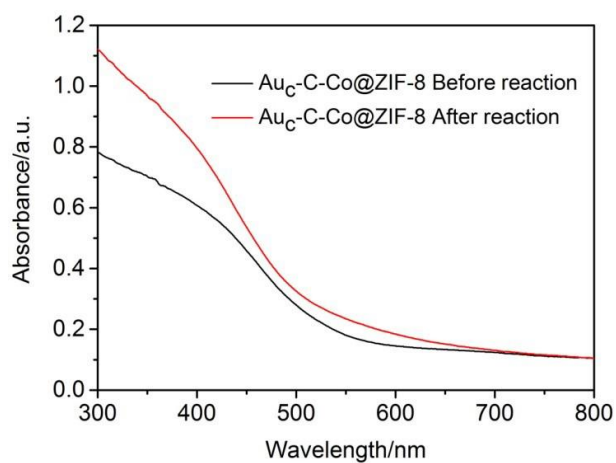


**Figure S21.** UV-vis absorption spectra of  $\text{Au}_x\text{-C-Co@ZIF-8}$  before and after 12-hour photocatalytic  $\text{CO}_2$  reduction.

As indicated by UV-vis absorption spectra (Figure S21), no SPR peak for Au nanoparticles can be observed after the 12-hour photocatalytic  $\text{CO}_2$  reduction. This suggests that Au NCs are well maintained after the photocatalytic reaction.

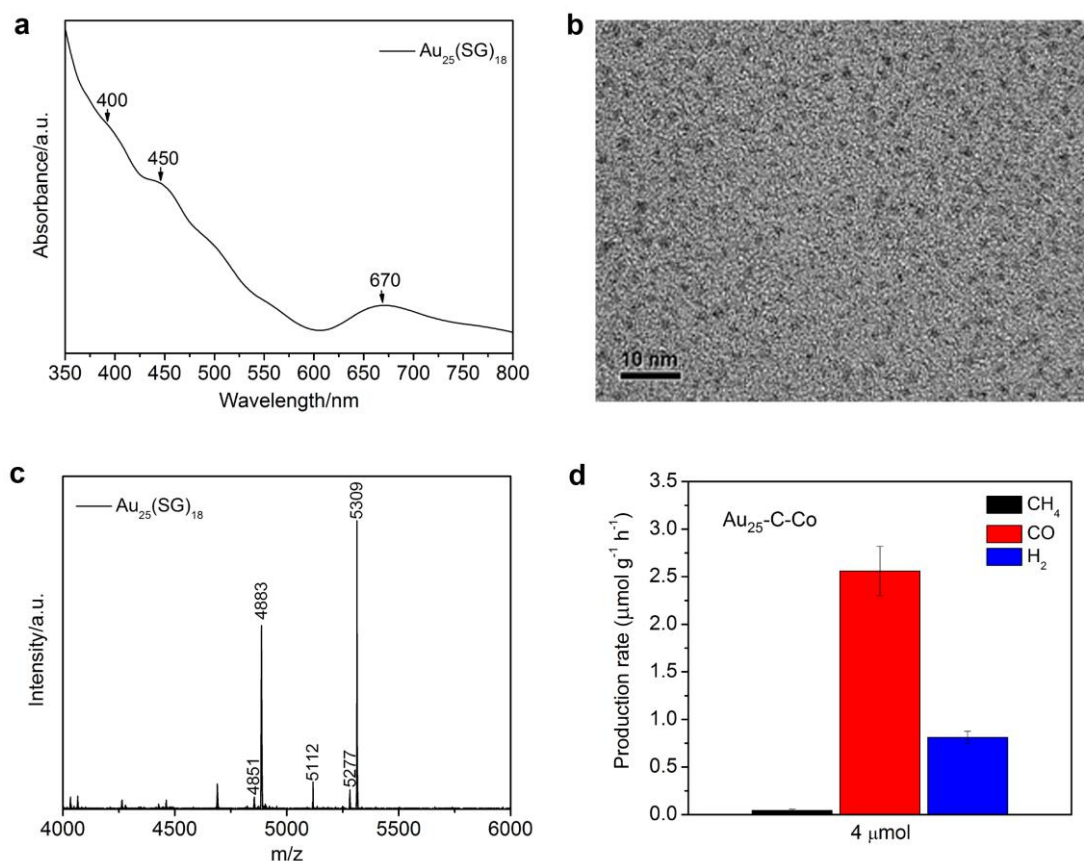


**Figure S22.** (a) UV-vis absorption spectrum, (b) TEM image and (c) MALDI-TOF mass spectrum of  $\text{Au}_{25}(\text{SG})_{18}$  NCs. (d) Average production rates of  $\text{CH}_4$ ,  $\text{CO}$  and  $\text{H}_2$  in light-driven  $\text{CO}_2$  reduction with  $\text{H}_2\text{O}$  in the presence of TEOA, catalyzed by 10-mg  $\text{Au}_{25}(\text{SG})_{18}$  NCs modified with L-cys and grafted with 4  $\mu\text{mol}$   $\text{Co}^{2+}$  ( $\text{Au}_{25}\text{-C-Co}$ ).

UV-vis absorption spectrum (Figure S22a) shows the characteristic absorption bands at 400, 450 and 670 nm, which are the spectroscopic fingerprints for thiol-capped  $\text{Au}_{25}$  nanoclusters.<sup>S2, S3</sup> TEM image (Figure S22b) reveals that the  $\text{Au}_{25}(\text{SG})_{18}$  NCs have an average size of *ca.* 1.1 nm.

MALDI-TOF mass spectrometry is further employed to confirm the core nature of  $\text{Au}_{25}(\text{SG})_{18}$  NCs with  $\alpha$ -cyano-4-hydroxycinnamic acid as the matrix. As shown in Figure S18c, no intact molecular ion peak for  $\text{Au}_{25}(\text{SG})_{18}$  is observed. Instead, only  $[\text{Au}_m\text{S}_n]^-$  fragments appear in the spectrum. The fragment peaks distribute with

spacing of  $m/z$  32, 197 or 229, corresponding to the loss of S, Au or AuS, respectively. The major peaks at  $m/z = 5309$ , 5112 and 4883 can be assigned to  $[\text{Au}_{25}\text{S}_{12}]^-$ ,  $[\text{Au}_{24}\text{S}_{12}]^-$  and  $[\text{Au}_{23}\text{S}_{11}]^-$ , respectively, consistent with the previous reports.<sup>S2</sup>

After modified with L-cys and grafted with  $\text{Co}^{2+}$ , the  $\text{Au}_{25}\text{-C-Co}$  shows good photocatalytic activity (Figure S22d), demonstrating that our reported approach should be applicable to various NCs.

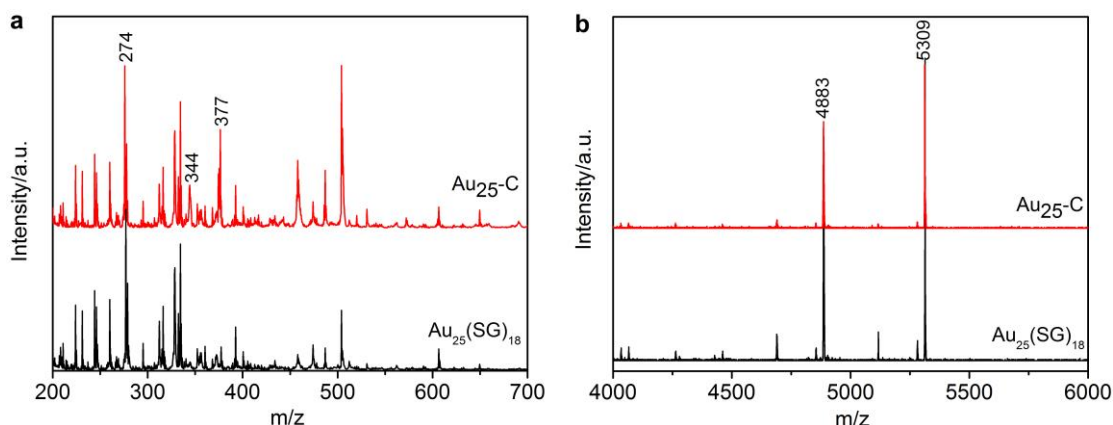


**Figure S23.** MALDI-TOF mass spectrum of Au<sub>25</sub>(SG)<sub>18</sub> NCs (lower) and those modified with L-cys (Au<sub>25</sub>-C) (upper) in different m/z range: (a) 200–700 and (b) 4000–6000.

We examine the grafting of L-cys to Au NCs based on a monodispersed Au<sub>25</sub>(SG)<sub>18</sub> system (Figure S23). Since the laser irradiation of MALDI-TOF cleaves the S–C bond of ligands, no intact molecular ion peak for Au<sub>25</sub>(SG)<sub>18</sub> or L-cys-modified Au<sub>25</sub>(SG)<sub>18</sub> (Au<sub>25</sub>-C) can be observed. As such, it is quite challenging to quantitatively identify how many L-cys molecules have been grafted onto the Au NCs. However, the two peaks at m/z = 344 and 377 observed for Au<sub>25</sub>-C may originate from the fragments of L-cys coupled with GSH after removing one or two thiols. This implies that the L-cys has been grafted onto the GSH. The characteristic peaks of Au<sub>25</sub>(SG)<sub>18</sub> at m/z = 274, 5309, 5112 and 4883 for thiol-removed GSH, [Au<sub>25</sub>S<sub>12</sub>]<sup>−</sup>, [Au<sub>24</sub>S<sub>12</sub>]<sup>−</sup> and [Au<sub>23</sub>S<sub>11</sub>]<sup>−</sup> remain mostly unchanged after the modification with L-cys, indicating that Au<sub>25</sub>(SG)<sub>18</sub> is well maintained during the functionalization.

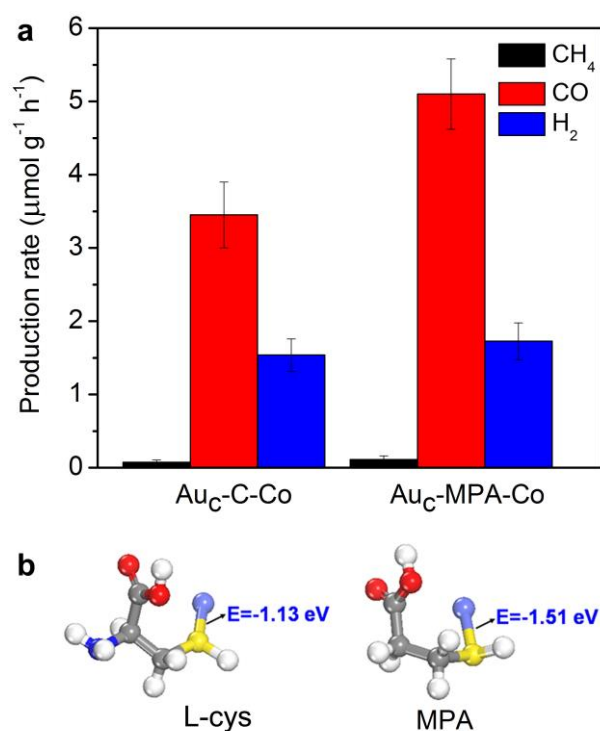


**Figure S24.** (a) Average production rates of CH<sub>4</sub>, CO and H<sub>2</sub> in light-driven CO<sub>2</sub> reduction with H<sub>2</sub>O in the presence of TEOA, catalyzed by 10-mg Au<sub>C</sub>-MPA-Co grafted with 4 μmol Co<sup>2+</sup>. (b) The binding energy of S-Co bond in the coordination of Co with L-cys and MPA.

To demonstrate the universal feature of our method, we modify Au-GSH NCs with 3-mercaptopropionic acid (MPA) ligands, and then graft Co<sup>2+</sup> onto the NCs through MPA. The obtained Au<sub>C</sub>-MPA-Co shows good activity for light-driven CO<sub>2</sub> reduction (Figure 24a), indicating that MPA also can work as an electron transporter.

We compare the photocatalytic activity of Au<sub>C</sub>-C-Co and Au<sub>C</sub>-MPA-Co, and identify that the activity of Au<sub>C</sub>-MPA-Co is slightly higher than that of Au<sub>C</sub>-C-Co. The molecular structure of MPA is quite similar to that of L-cys except the absence of amine in MPA, resulting in their different charge densities of thiols. The nitrogen atom possesses a stronger negative induction effect owing to its high electronegativity than sulfur, which makes the charge density of thiol in L-cys lower than that in MPA.



DFT calculation (Figure 24b) reveals that the binding energy of S–Co in the coordination of L-cys with Co (-1.13 eV) is lower than that for MPA (-1.51 eV). We assume that the stronger S–metal cation interaction promotes the photocatalytic activity.

**Table S1.** Activity and selectivity for the light-driven reduction of CO<sub>2</sub>, catalyzed by Au NCs-based catalysts. No other products have been detected in the reactions.

Catalysts	Average production rate ( $\mu\text{mol}\cdot\text{g}_{\text{cat}}^{-1}\cdot\text{h}^{-1}$ ) <sup>a</sup>			$R_{\text{electron}}$ ( $\mu\text{mol}\cdot\text{g}_{\text{cat}}^{-1}\cdot\text{h}^{-1}$ ) <sup>b</sup>	Selectivity(%) <sup>c</sup>		
	CH <sub>4</sub>	CO	H <sub>2</sub>		CH <sub>4</sub>	CO	H <sub>2</sub>
Au-GSH NCs	N.d. <sup>d</sup>	N.d.	N.d.	—	—	—	—
Au-GSH NCs+M	N.d.	N.d.	N.d.	—	—	—	—
Au <sub>c</sub> -C	N.d.	N.d.	N.d.	—	—	—	—
Au <sub>c</sub> -C-Co (1 $\mu\text{mol}^e$ )	0.037 $\pm 0.04$	2.392 $\pm 0.14$	0.751 $\pm 0.11$	6.584	4.52	72.66	22.82
Au <sub>c</sub> -C-Co (2 $\mu\text{mol}$ )	0.040 $\pm 0.03$	2.930 $\pm 0.19$	0.928 $\pm 0.15$	8.037	3.99	72.92	23.09
Au <sub>c</sub> -C-Co (4 $\mu\text{mol}$ )	0.075 $\pm 0.03$	3.451 $\pm 0.45$	1.539 $\pm 0.22$	10.582	5.70	65.22	29.08
Au <sub>c</sub> -C-Co (8 $\mu\text{mol}$ )	0.042 $\pm 0.02$	1.689 $\pm 0.17$	1.065 $\pm 0.19$	5.847	5.80	57.77	36.43
Au <sub>c</sub> -C-Co (12 $\mu\text{mol}$ )	0.018 $\pm 0.02$	0.749 $\pm 0.15$	1.189 $\pm 0.24$	4.017	3.54	37.27	59.20
Au <sub>c</sub> -C-Co (16 $\mu\text{mol}$ )	0.000	0.201 $\pm 0.11$	0.791 $\pm 0.21$	1.983	0.00	20.26	79.74
Au <sub>c</sub> -C-Co (20 $\mu\text{mol}$ )	0.000	0.070 $\pm 0.04$	0.220 $\pm 0.09$	0.580	0.00	24.14	75.86
Au <sub>c</sub> -C-Fe (4 $\mu\text{mol}$ )	0.095 $\pm 0.08$	0.314 $\pm 0.21$	2.979 $\pm 0.45$	7.346	10.35	8.54	81.11
Au <sub>c</sub> -C-Ni (4 $\mu\text{mol}$ )	0.042 $\pm 0.02$	0.685 $\pm 0.12$	14.700 $\pm 1.20$	31.109	1.09	4.40	94.51
Au <sub>c</sub> -C-Cu (4 $\mu\text{mol}$ )	0.000	0.000	2.205 $\pm 0.41$	4.410	0	0	100

<sup>a</sup>Reaction conditions: 10 mg of catalysts in aqueous TEOA solution (10% v/v); 100 mW cm<sup>-2</sup>; visible light ( $\lambda \geq 420$  nm); 3 h. <sup>b</sup> $R_{\text{electron}}$  is the rate of electron consumption for reduction products;  $R_{\text{electron}} = 2\nu(\text{CO}) + 8\nu(\text{CH}_4) + 2\nu(\text{H}_2)$ . <sup>c</sup>The selectivity of reduction products is evaluated based on the required electrons using the following equation: Selectivity (CO)% =  $[2\nu(\text{CO})]/[2\nu(\text{CO}) + 8\nu(\text{CH}_4) + 2\nu(\text{H}_2)] \times 100$ , Selectivity (CH<sub>4</sub>)% =  $[8\nu(\text{CH}_4)]/[2\nu(\text{CO}) + 8\nu(\text{CH}_4) + 2\nu(\text{H}_2)] \times 100$ , and Selectivity

$(\text{H}_2)\% = [2\nu(\text{H}_2)]/[2\nu(\text{CO}) + 8\nu(\text{CH}_4) + 2\nu(\text{H}_2)] \times 100$ , where  $\nu(\text{H}_2)$ ,  $\nu(\text{CO})$  and  $\nu(\text{CH}_4)$  stand for the formation rates for  $\text{H}_2$ ,  $\text{CO}$  and  $\text{CH}_4$ , respectively. <sup>d</sup>Not detected.  
<sup>e</sup>The amount of added metal cations.

**Table S2.** The amount of metal cations grafted to 10 mg of Au<sub>c</sub>-C, determined by ICP-OES.

Samples	Amount of metal cations (μmol)			
	Fe	Co	Ni	Cu
Au <sub>c</sub> -C-Fe	3.17	—	—	—
Au <sub>c</sub> -C-Co	—	2.41	—	—
Au <sub>c</sub> -C-Ni	—	—	1.34	—
Au <sub>c</sub> -C-Cu	—	—	—	3.45

The measurement method is the same as that for Figure S3.

**Table S3.** A summary of the photocatalytic performances for CO<sub>2</sub> reduction by various visible-light-responsive catalysts.

Catalyst	Products	$R_{\text{electron}}$ ( $\mu\text{mol}\cdot\text{g}_{\text{cat}}^{-1}\cdot\text{h}^{-1}$ )	Incident light	Ref.
Au <sub>c</sub> -C-Co	CH <sub>4</sub> , CO, H <sub>2</sub>	10.6	$\lambda \geq 420$ nm 100 mW·cm <sup>-2</sup>	This work
Au <sub>c</sub> -C-Ni	CH <sub>4</sub> , CO, H <sub>2</sub>	31.1	$\lambda \geq 420$ nm 100 mW·cm <sup>-2</sup>	This work
CrPbBr <sub>3</sub> /GO	CH <sub>4</sub> , CO, H <sub>2</sub>	29.8	AM 1.5G 150 mW·cm <sup>-2</sup>	S14
CdS	HCOO <sup>-</sup> , CO, H <sub>2</sub>	0.977	$\lambda \geq 300$ nm 1000 mW·cm <sup>-2</sup>	S15
CdS-WO <sub>3</sub>	CH <sub>4</sub>	8.16	$\lambda \geq 420$ nm 150 mW·cm <sup>-2</sup>	S16
RGO-CdS	CH <sub>4</sub>	20.1	$\lambda \geq 420$ nm 150 mW cm <sup>-2</sup>	S17
Bi <sub>2</sub> WO <sub>6</sub>	CH <sub>4</sub>	8.8	$\lambda \geq 420$ nm	S18
BiVO <sub>4</sub>	CH <sub>3</sub> OH	33.12	$\lambda \geq 420$ nm	S19
g-C <sub>3</sub> N <sub>4</sub> -NH <sub>2</sub>	CH <sub>4</sub> , CH <sub>3</sub> OH	5		S20
N-TiO <sub>2</sub>	CH <sub>3</sub> OH	1.68	$\lambda \geq 400$ nm	S21

**Table S4.** The fitting parameters for the PL decay curves of Au<sub>c</sub>-C grafted with different metal cations (Fe<sup>2+</sup>, Co<sup>2+</sup>, Ni<sup>2+</sup> and Cu<sup>2+</sup>) in aqueous solution.

Samples	A <sub>1</sub>	A <sub>2</sub>	A <sub>3</sub>	τ <sub>1</sub> (ns)	τ <sub>2</sub> (ns)	τ <sub>3</sub> (ns)	T <sub>average</sub> (ns)
Au <sub>c</sub> -C-Fe	0.18	2.84 × 10 <sup>-3</sup>	18.89	1.77	13.4	4.44 × 10 <sup>-2</sup>	3.17
Au <sub>c</sub> -C-Co	0.34	1.11 × 10 <sup>-3</sup>	7.41	1.63	11.3	3.23 × 10 <sup>-2</sup>	0.51
Au <sub>c</sub> -C-Ni	0.61	1.13 × 10 <sup>-3</sup>	20.17	0.19	17.2	1.36 × 10 <sup>-2</sup>	0.89
Au <sub>c</sub> -C-Cu	7.17 × 10 <sup>-3</sup>	8.13 × 10 <sup>-3</sup>	87.81	0.06	3.94	2.73 × 10 <sup>-2</sup>	0.08

Au<sub>c</sub>-C-Cu, Au<sub>c</sub>-C-Co and Au<sub>c</sub>-C-Ni show fast decay with average PL decay time (T<sub>average</sub>) of 0.08 ns, 0.51 ns and 0.89 ns, respectively, while Au<sub>c</sub>-C-Fe exhibits comparable T<sub>average</sub> to Au<sub>c</sub>-C. Nevertheless, electron transfer is not the only factor responsible for PL decay. The contributions of τ<sub>1</sub> and τ<sub>2</sub> are more related to charge transfer. Although the τ<sub>1</sub> and τ<sub>2</sub> for Au<sub>c</sub>-C-Cu are smaller than those for Au<sub>c</sub>-C-Co, its PL decay is more governed by τ<sub>3</sub>.

## References:

- [S1] Luo, Z. T.; Yuan, X.; Yu, Y.; Zhang, Q. B.; Leong, D. T.; Lee, J. Y.; Xie, J. P. *J. Am. Chem. Soc.* **2012**, *134*, 16662.
- [S2] Luo, Y.; Fan, S.; Yu, W.; Wu, Z. D.; Cullen, A.; Liang, C.; Shi, J.; Su, C. *Adv. Mater.* **2017**, *29*, 1704576.
- [S3] Negishi, Y.; Nobusada, K.; Tsukuda, T. *J. Am. Chem. Soc.* **2005**, *127*, 5261.
- [S4] Xu, Y. F.; Yang, M. Z.; Chen, B. X.; Wang, X. D.; Chen, H. Y.; Kuang, D. B.; Su, C. Y. *J. Am. Chem. Soc.* **2017**, *139*, 5660.
- [S5] Lightcap, I. V.; Kamat, P. V. *J. Am. Chem. Soc.* **2012**, *134*, 7109.
- [S6] Kresse, G.; Furthmüller, J. *Phys. Rev. B* **1996**, *54*, 11169.
- [S7] Kresse, G.; Furthmüller, J. *Comput. Mater. Sci.* **1996**, *6*, 15.
- [S8] Blöchl, P. E. *Phys. Rev. B* **1994**, *50*, 17953.
- [S9] Perdew, J. P.; Burke, K.; Ernzerhof, M. *Phys. Rev. Lett.* **1996**, *77*, 3865.
- [S10] Henkelman, G.; Jonsson, H. *J. Chem. Phys.* **2000**, *113*, 9978.
- [S11] Henkelman, G.; Uberuaga, B. P.; Jonsson, H. *J. Chem. Phys.* **2000**, *113*, 9901.
- [S12] Liu, B.; Zhao, Z.; Henkelman, G.; Song, W. *J. Phys. Chem. C* **2016**, *120*, 5557.
- [S13] Lu, Y.; Zhang, R.; Cao, B.; Ge, B.; Tao, F. F.; Shan, J.; Nguyen, L.; Bao, Z.; Wu, T.; Pote, J. W.; Wang, B.; Yu, F. *ACS Catal.* **2017**, *7*, 5500.
- [S14] Xu, Y. F.; Yang, M. Z.; Chen, B. X.; Wang, X. D.; Chen, H. Y.; Kuang, D. B.; Su, C. Y. *J. Am. Chem. Soc.* **2017**, *139*, 5660.
- [S15] Liu, B. J. *J. Photochem. Photobiol. A* **1998**, *113*, 93.
- [S16] Jin, J.; Yu, J.; Guo, D.; Cui, C.; Ho, W. *Small* **2015**, *11*, 5262.
- [S17] Yu, J.; Jin, J.; Cheng, B.; Jaroniec, M. *J. Mater. Chem. A* **2014**, *2*, 340.
- [S18] Zhou, Y.; Tian, Z.; Zhao, Z.; Liu, Q.; Kou, J.; Chen, X.; Gao, J.; Yan, S.; Zou, Z. *ACS Appl. Mater. Interfaces* **2011**, *3*, 3594.
- [S19] Mao, J.; Peng, T.; X.; Zhang; Li, K.; Zan, L. *Catal. Commun.* **2012**, *28*, 38.
- [S20] Huang, Q.; Yu, J.; Cao, S.; Cui, C.; Cheng, B. *Appl. Surf. Sci.* **2015**, *358*, 350.
- [S21] Maxwell, S. A.; Low, J.; Qin, Z.; Wageh, S.; Al-Ghamdi, A. A.; Yu, J.; Liu, S. *Chin. J. Catal.* **2015**, *36*, 2127.